

# MATCHA: MULTI-STAGE RIEMANNIAN FLOW MATCHING FOR ACCURATE AND PHYSICALLY VALID MOLECULAR DOCKING

**Anonymous authors**

Paper under double-blind review

## ABSTRACT

Accurate prediction of protein-ligand binding poses is crucial for structure-based drug design, yet existing methods struggle to balance speed, accuracy, and physical plausibility. We introduce MATCHA, a novel molecular docking pipeline that combines multi-stage flow matching with learned scoring and physical validity filtering. Our approach consists of three sequential stages applied consecutively to progressively refine docking predictions, each implemented as a flow matching model operating on appropriate geometric spaces ( $\mathbb{R}^3$ ,  $SO(3)$ , and  $SO(2)$ ). We enhance the prediction quality through a dedicated scoring model and apply unsupervised physical validity filters to eliminate unrealistic poses. Compared to various approaches, MATCHA demonstrates superior performance on ASTEX and PDBBIND test sets in terms of docking success rate and physical plausibility. Moreover, our method works approximately  $25\times$  faster than modern large-scale co-folding models.

## 1 INTRODUCTION

Molecular docking aims to predict the binding pose of a small molecule (ligand) within the active site of a target protein. It plays a key role in computer-aided drug discovery, particularly in virtual screening, the computational search for promising drug candidates within large-scale compound libraries. Given the vast size of these libraries, practical docking methods must balance accuracy with computational efficiency. Additionally, predicted poses are expected to be physically plausible (Buttenschoen et al., 2024). Another challenge is the diversity of existing docking benchmarks, which differ substantially in target and ligand selection, making it difficult to design methods that generalize well across all datasets.

Classical docking approaches (Friesner et al., 2004; Trott & Olson, 2010; Koes et al., 2013; Forli et al., 2016; Sulimov et al., 2020) have traditionally relied on hand-crafted scoring functions combined with heuristic search algorithms. However, recent benchmarks (Morehead et al., 2025) demonstrate that such methods are outperformed by data-driven approaches.

Modern data-driven blind docking methods (Abramson et al., 2024; Boitreaud et al., 2024; Wohlwend et al., 2024), starting from the seminal DIFFDOCK (Corso et al., 2022), typically formulate molecular docking as a generative modeling problem, where a neural network — often a diffusion model — learns to sample ligand poses from a probabilistic distribution.

Our proposed method, MATCHA, follows this generative paradigm but is based on flow MATCHING (Lipman et al., 2022) rather than diffusion. Following DIFFDOCK, we represent ligand flexibility in a joint space of translations, global rotations, and internal torsions. This corresponds to a semi-flexible ligand: the conformation is fixed except for rotations around rotatable bonds. In contrast to Riemannian diffusion-based methods, Riemannian flow matching (Chen & Lipman, 2023) provides tractable losses in these spaces and simplifies training. Moreover, our approach naturally bypasses the need for semi-flexible conformational alignment, which is a challenging optimization problem. To the best of our knowledge, it is the first docking pipeline that is built upon flow matching on non-Euclidean manifolds.

Architecturally, MATCHA combines the structure of a Diffusion Transformer (DiT; Peebles & Xie 2023) with a spatial encoder inspired by UNIMOL (Zhou et al., 2023). Our pipeline consists of three neural networks trained at different noise levels. For instance, the first model is optimized to predict the 3D translational displacement of the ligand center relative to the binding site. By default, MATCHA is trained for blind docking, but the pocket-informed setting can be managed by omitting the coarse model and providing the correct binding site location. Also, we train a separate scoring model to select the best pose among all generated candidates.

Our main contributions are as follows:

- We introduce MATCHA, a neural pipeline for molecular docking that combines Riemannian flow matching with a DiT-inspired architecture. The pipeline employs three neural networks applied consecutively to refine docking predictions progressively.
- We perform an extensive empirical evaluation of MATCHA against state-of-the-art methods, comparing binding quality, computational efficiency, and physical plausibility across the PDBBIND, DOCKGEN, ASTEX, and POSEBUSTERS V2 benchmarks.
- MATCHA achieves inference approximately  $25\times$  faster than ALPHAFOLD 3, CHAI-1, and BOLTZ-2, while having state-of-the-art docking performance on the ASTEX test set: 66% with  $\text{RMSD} \leq 2 \text{ \AA}$  & PB-valid (Buttenschoen et al., 2024) and competitive results on other benchmarks.

## 2 METHOD

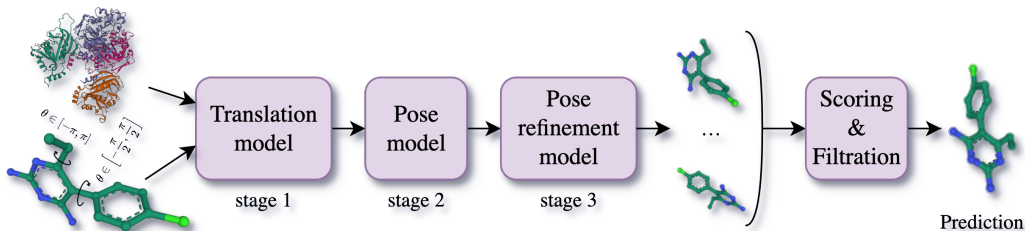


**Figure 1:** MATCHA consists of three flow matching models that generate a set of ligand poses. After unsupervised physical validity filtration, all poses are scored with a separate model, and the prediction is the pose with the best score. We highlight rotatable bonds and their periods in the ligand on this figure.

### 2.1 DOCKING LOSS FUNCTION

MATCHA tackles the molecular docking problem by modeling a protein as a rigid body while parameterizing the ligand’s degrees of freedom in a manner similar to DIFFDOCK. Specifically, we operate in the following spaces:

- **translation (tr):** a 3D continuous vector representing the position of the ligand’s center relative to the protein,
- **rotation (rot):** an  $\text{SO}(3)$  transformation matrix representing the orientation of ligand,
- **torsion angles (tor):** a set of angles in  $\text{SO}(2)$ , one for each rotatable bond in the ligand.

For rotatable bonds, we define the torsional period  $p$  as the smallest positive angle such that a rotation by  $p$  about that bond yields an indistinguishable configuration (up to symmetry). Accordingly, torsion angles are taken modulo  $p$ , i.e., for any  $\theta$  we use its wrapped representative  $\theta \bmod p$  that is in  $(-p/2, p/2]$ .

Our model predicts velocities  $\mathbf{v}_{\text{tr}}$ ,  $\mathbf{v}_{\text{rot}}$ , and  $\mathbf{v}_{\text{tor}}$  in the tangent spaces  $\mathbb{R}^3$ ,  $\mathfrak{so}(3)$ , and  $\mathfrak{so}(2)^m$ , with  $m$  denoting the number of rotatable bonds. Elements of  $\mathfrak{so}(n)$  can be thought of as  $n \times n$  real skew-symmetric matrices (Warner, 1983), we represent them as  $n(n-1)/2$ -dimensional vectors.

We compute separate flow matching losses (Chen & Lipman, 2023) for each component and optimize their weighted sum. Generally, to train a flow matching model  $v_\theta$  given data points  $x_1$  on a Riemannian manifold  $\mathcal{M}$  drawn from  $p_{\text{data}}$ , we should define a noise distribution  $p_0$ . Then we choose an interpolation on  $\mathcal{M}$ , select an appropriate norm, and compute the time derivative of the interpolation to obtain the conditional velocity. The conditional flow matching loss takes the form:

$$\mathcal{L}_{\text{CFM}} = \mathbb{E}_{x_0 \sim p_0, x_1 \sim p_{\text{data}}, t \sim \mathcal{U}[0,1]} \|v_\theta(x_t, t) - \dot{x}_t\|, \text{ where } x_t = \text{interpolate}(x_0, x_1; t). \quad (1)$$

For translations, we use a standard linear interpolation and normally distributed noise. For both angular components, we adopt spherical linear interpolation (SLERP; Shoemake 1985). In  $\text{SO}(3)$ , the time derivative of SLERP is computed by transforming to quaternion representations and applying automatic differentiation with custom backward functions. Additional derivation details are provided in Appendix A.

## 2.2 ARCHITECTURE

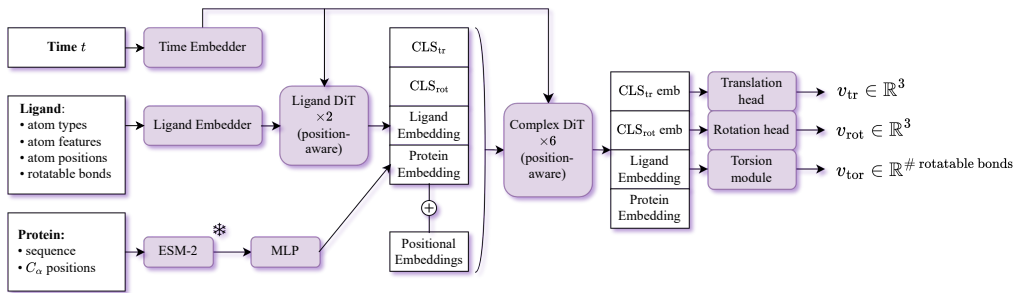


**Figure 2:** The architecture of the velocity model of MATCHA (stages 1, 2, 3).

MATCHA consists of two primary components (Figure 1): the docking pipeline and the scoring model. These components are implemented through a transformer-based architecture and have a similar design (Figure 2).

### 2.2.1 VELOCITY MODEL

**Input tokens** The input sequence consists of ligand atom tokens, protein amino acid residue tokens, and two CLS-like tokens for aggregating translation (CLS<sub>tr</sub>) and global rotation (CLS<sub>rot</sub>) information. Each token is assigned a 3D coordinate: atom positions for ligand atoms,  $C_\alpha$  positions for residues, and the ligand centroid for both CLS tokens. Protein representations are initialized from ESM-2-35M (Lin et al., 2022) embeddings; we use the 35M model instead of the 650M variant to reduce the risk of overfitting. Initial ligand atom embeddings are a sum of simple embeddings of scalar and categorical atom features from the RDKit package (Landrum, 2024).

Time  $t \in [0, 1]$  is embedded by an MLP over sinusoidal features and conditions all transformer blocks in a DiT-like manner. Positions  $(x, y, z)$  are encoded using a simple MLP and added to both embeddings of ligand atoms and protein residues in a manner of positional encoding in transformers.

**Distance-aware attention bias** We adopt the approach from UNIMOL and ALPHAFOLD 3, where spatial features are used as extra biases in self-attention. Given 3D coordinates  $x = \{x_i\}_{i=1}^N$ ,  $x_i \in \mathbb{R}^3$ , we form a per-head attention bias by combining a radial (distance-based) and a directional (vector-based) term. For a pair  $(i, j)$  with edge type  $t_{ij} \in \{1, \dots, T\}$ , define the displacement  $\Delta_{ij} = x_i - x_j$  and a stabilized inverse distance

$$s_{ij} = \frac{1}{\|\Delta_{ij}\|_2^2 + 1}. \quad (2)$$

An edge-type-specific affine transform produces  $\tilde{s}_{ij} = \alpha_{t_{ij}} s_{ij} + \beta_{t_{ij}}$ . We then embed  $\tilde{s}_{ij}$  with a  $K$ -kernel Gaussian RBF:

$$\phi_{ij}^{(k)} = \mathcal{N}(\tilde{s}_{ij}; \mu_k, \sigma_k^2), \quad k = 1, \dots, K, \quad (3)$$

162 followed by a small MLP projection  $g : \mathbb{R}^K \rightarrow \mathbb{R}^H$  to obtain a per-head radial bias  $o_{ij} = g(\phi_{ij}) \in$   
 163  $\mathbb{R}^H$ . In parallel, a directional projection  $h : \mathbb{R}^3 \rightarrow \mathbb{R}^H$  maps the displacement to  $v_{ij} = h(\Delta_{ij})$ . The  
 164 per-pair bias is  $b_{ij} = g(\phi_{ij}) + h(\Delta_{ij}) \in \mathbb{R}^H$ . Stacking over all pairs yields a tensor in  $\mathbb{R}^{N \times N \times H}$ ;  
 165 we then move the head dimension to the front to obtain  $B_{hij} = [b_{ij}]_h \in \mathbb{R}^{H \times N \times N}$ , which we add  
 166 to the attention logits.  
 167

168 **Velocity prediction heads** After the transformer backbone, we employ lightweight modules to  
 169 predict the velocity fields. We do not force rotational or translational symmetries via the architecture;  
 170 instead, we rely on data augmentations during training to promote invariances and equivariances.  
 171

172 The translation head consumes the dedicated  $\text{CLS}_{\text{tr}}$  token and outputs a 3D velocity vector  $v_{\text{tr}} \in \mathbb{R}^3$ .  
 173 The rotation head consumes the  $\text{CLS}_{\text{rot}}$  token and outputs a 3-vector representation of  $\mathfrak{so}(3)$ . For  
 174 torsions, we construct a token for each rotatable bond by averaging the embeddings of ligand atoms  
 175 influenced by the rotation of that bond and combining this with an encoding of basic features of the  
 176 bond level. The resulting per-bond sequence is passed through a lightweight transformer decoder,  
 177 and a final single-layer MLP projects each token to a scalar torsional velocity  $v_{\text{tor}}$ .

178 **Coarse-to-fine structure** Our pipeline stacks three models of identical architecture but indepen-  
 179 dent weights. The first model is used solely for translation, where samples are drawn from a zero-  
 180 mean Gaussian distribution with a large variance, while angular components are sampled uniformly.  
 181 The second model refines translation using a Gaussian centered at the ground truth with moderate  
 182 variance, still keeping angular components uniform. Finally, the third model sharpens both transla-  
 183 tion and angular degrees of freedom, sampling them from Gaussians with small variance around the  
 184 ground truth. The models are trained independently. Full details are provided in Algorithm 1.

185 The system can operate in two distinct scenarios: blind docking and pocket-aware docking. Blind  
 186 docking means predicting ligand poses without prior knowledge of the binding site location, while  
 187 in the pocket-aware scenario, the information about the known binding site is used to guide pose  
 188 prediction. This flexibility is achieved because of the multiscale nature of MATCHA.  
 189

190 **Augmentations** During training, we apply multiple augmentation techniques to avoid overfitting  
 191 and improve model generalization. Firstly, we randomly rotate the whole complex to get new  
 192  $(x, y, z)$  coordinates. Secondly, we add random Gaussian noise with zero mean and standard de-  
 193 viation 0.25 to the protein and ligand positions. Finally, we randomly mask 15% of protein residues  
 194 and ligand atoms. This strategy also leads to masking of some rotatable bonds.  
 195

196 **Inference** We run a fixed-length explicit Riemannian Euler solver (10 steps) over  $(\text{tr}, \text{rot}, \text{tor})$   
 197 using the predicted velocities, applying three models sequentially.  
 198

199 Stage 1 From a random initialization, we integrate all degrees of freedom (translation, rotation,  
 200 torsions), but retain only the predicted translation; the angular components are discarded  
 201 and reinitialized uniformly.

202 Stage 2 Starting from this state (predicted translation and uniformly distributed angles), we perform  
 203 the same rollout and pass the full output  $(\text{tr}, \text{rot}, \text{tor})$  forward.

204 Stage 3 We execute the final rollout to produce the refined pose.  
 205

## 206 2.2.2 POSE SELECTION

208 **Scoring model** We train a separate pose-scoring network to evaluate and rank candidate docking  
 209 poses. It shares the backbone with our docking model but removes time conditioning and all flow  
 210 matching components. Instead, a dedicated scalar scoring head is optimized with an RMSD-based  
 211 pairwise ranking objective for comparative pose assessment. For training, each batch is composed of  
 212 multiple noisy poses of the same protein-ligand complex, and the model learns to order the resulting  
 213 pairs of poses.  
 214

215 **Pose filtration** We reimplement, speed up, and apply a minimal set of PoseBusters geometric and  
 physicochemical validity filters before scoring. Specifically, we retain candidate complexes that

**Algorithm 1:** General scheme of MATCHA docking training

---

**Input:** Protein-ligand complexes  $D$ , initialized flow model  $v$ , stage  $\in \{1, 2, 3\}$ ,  $\sigma_{\text{large}}$ ,  $\sigma_{\text{medium}}$ ,  $\sigma_{\text{small}}$   
**for** batch of ligand-protein complexes in  $D$  **do**

1. Take conformation of ligand from batch. Compute the centroid  $\text{tr}_{\text{true}}$  of this conformation. Apply augmentations (Section 2.2.1, augmentations).
2. Identify rotatable bonds and define their quantity by  $m$ .
3. Sample random translation, rotation, and torsion:  $\text{tr}$ ,  $\text{rot}$ ,  $\text{tor}$  and apply them to the conformation.
4. Set  $\text{rot}_{\text{true}} := \text{inverse}(\text{rot})$ ,  $\text{tor}_{\text{true}} := \text{inverse}(\text{tor})$ .
5. Sample noise for translation, rotation, and torsion transformations  $\text{tr}_{\text{noise}}$ ,  $\text{rot}_{\text{noise}}$ ,  $\text{tor}_{\text{noise}}$ :
  - if stage = 1:  $\text{tr}_{\text{noise}} \sim \mathcal{N}(0, \sigma_{\text{large}}^2)$ ,  $\text{rot}_{\text{noise}} \sim \text{Unif}(\text{SO}(3))$ ,  $\text{tor}_{\text{noise}} \sim \text{Unif}(\text{SO}(2))^m$
  - if stage = 2:  $\text{tr}_{\text{noise}} \sim \mathcal{N}(\text{tr}_{\text{true}}, \sigma_{\text{medium}}^2)$ ,  $\text{rot}_{\text{noise}} \sim \text{Unif}(\text{SO}(3))$ ,  $\text{tor}_{\text{noise}} \sim \text{Unif}(\text{SO}(2))^m$
  - if stage = 3:  $\text{tr}_{\text{noise}} \sim \mathcal{N}(\text{tr}_{\text{true}}, \sigma_{\text{small}}^2)$ ,  $\text{rot}_{\text{noise}} \sim \mathcal{N}(\text{rot}_{\text{true}}, \sigma_{\text{small}}^2 \mathbf{I})$ ,  $\text{tor}_{\text{noise}} \sim \mathcal{N}(\text{tor}_{\text{true}}, \sigma_{\text{small}}^2)^m$
6. Sample  $t \sim \text{Uniform}(0, 1)$ , interpolate transformations between noisy ( $\text{tr}_{\text{noise}}$ ,  $\text{rot}_{\text{noise}}$ ,  $\text{tor}_{\text{noise}}$ ) and true values ( $\text{tr}_{\text{true}}$ ,  $\text{rot}_{\text{true}}$ ,  $\text{tor}_{\text{true}}$ ), and apply these transformations to the ligand conformation, resulting in  $\mathbf{x}(t) := (\text{tr}(t), \text{rot}(t), \text{tor}(t))$ .
7. Obtain the output of the flow model,  $v(\mathbf{x}(t), t)$ , which belongs to  $\mathbb{R}^3 \times \mathfrak{so}(3) \times \mathfrak{so}(2)^m$ .
8. Compute the flow matching loss for each component of  $v(\mathbf{x}(t), t)$  separately and compute their linear combination.
9. Execute the gradient optimization step of the computed loss.

**Output:** Trained flow model  $v$  for the given stage

---

achieve the highest filter scores across key validity criteria: (i) *Minimum distance to protein*, preventing ligand–receptor atomic collision; (ii) *Protein–ligand maximum distance*, excluding poses with excessive protein–ligand separation that are unlikely to form specific interactions; (iii) *Volume overlap with protein*, rejecting any nonzero volumetric overlap with the receptor; and (iv) *Internal steric clash*, removing ligand conformers with intramolecular clashes. Filtration is strictly unsupervised—i.e., it does not rely on knowledge of the native pose – and is therefore readily applicable at inference. In practice, for each complex we retain the poses that pass the highest number of validity criteria and then select a single pose using our learned scoring model.

### 3 EXPERIMENTAL SETUP

#### 3.1 DATASETS

MATCHA is trained on two major protein-ligand complex datasets: PDBBIND (Liu et al., 2017) and BINDING MOAD (Hu et al., 2005). During training, we keep only protein chains close to the ligand (less than 4.5 Å). **For both datasets, we use splits provided by (Corso et al., 2024). Additional MOAD complexes belong to pocket clusters of PDBBIND train set.** We use complexes that have proteins with less than 2000 residues and ligands with 6 – 150 heavy atoms. At training time, we concatenate the BINDING MOAD dataset to the PDBBIND training set without removing redundant complexes, thereby giving additional weight to higher-quality complexes that passed both datasets’ filtering processes.

For the BINDING MOAD dataset, we implement protein-level sampling to address the inherent class imbalance where multiple ligands are bound to the same protein structure. During every training epoch, we sample each unique protein exactly once. For each selected protein, we randomly choose one ligand from all ligands bound to that receptor.

The docking quality is evaluated on four test datasets. ASTEX Diverse set (Hartshorn et al., 2007) and POSEBUSTERS V2 Benchmark set (Buttenschoen et al., 2024) are commonly used in the field and contain 85 and 308 complexes, respectively. DOCKGEN (Corso et al., 2024) is a set of 330 hard complexes with binding sites different from the training set. Finally, we use the PDBBIND test set obtained using time-splitting of dataset complexes and has 363 complexes (Corso et al., 2022).

### 3.2 TRAINING DETAILS

All models are trained with the AdamW optimizer (Loshchilov & Hutter, 2017) using a learning rate of  $5 \times 10^{-5}$ . The docking models employ a batch size of 24 and are trained on a single NVIDIA H100 GPU (80GB). Stage 1 training runs for 1.9M steps ( $\approx 11$  days), stage 2 for 3.3M steps ( $\approx 19$  days), and stage 3 for 1.4M steps ( $\approx 8$  days), totaling 38 GPU-days. The scoring model is trained separately with batch size 12 on an NVIDIA V100 GPU (16GB) for 700k steps ( $\approx 26$  hours).

All MATCHA models use 6 Complex DiT layers with hidden dimension 192. This corresponds to  $\sim 29$ M parameters for the docking models and  $\sim 6$ M parameters for the scoring model. For docking, we optimize a weighted objective with loss coefficients  $w_{\text{tr}} = 1$ ,  $w_{\text{rot}} = 1$ , and  $w_{\text{tor}} = 3$ .

### 3.3 DOCKING QUALITY METRICS

To comprehensively evaluate the performance of MATCHA, we use symmetry-corrected Root Mean Square Deviation (RMSD) that accounts for molecular symmetry and report success rates at  $2 \text{ \AA}$  threshold ( $\text{RMSD} \leq 2 \text{ \AA}$ ). We also run POSEBUSTERS tests (Buttenschoen et al., 2024) to assess physical plausibility of predicted poses, resulting in the combined metric  $\text{RMSD} \leq 2 \text{ \AA}$  & PB-valid. Exact POSEBUSTERS tests are listed in Appendix I. For models that predict whole complex structures, we follow Abramson et al. (2024) and use pocket-aligned symmetric RMSD by aligning the reference protein pocket to the predicted structure. If a model crashes on a complex, we assign an RMSD of  $+\infty$ . The details are reported in Section 4.5 and Appendix G.1.

### 3.4 HOW WE RUN BASELINES

**Baseline model parameters** For ALPHAFOLD 3 (Abramson et al., 2024), BOLTZ-2 (Passaro et al., 2025) and CHAI-1 (Boitreaud et al., 2024), we use the prediction with the highest confidence score among five model seeds with five samples per seed and 10 recycling steps. We used multiple sequence alignments computed with JACKHMMER (HMMER3) (Eddy, 2011). When modeling receptor structures, we preserve all chains and remove exact duplicate chains only. NEURALPLEXER (Qiao et al., 2024b), DIFFDOCK-L (Corso et al., 2024) and UNI-MOL (Alcaide et al., 2024) are run with their default inference parameters. We run FLOWDOCK (Morehead & Cheng, 2025) using true holo protein structures as receptor templates. For all methods, we take the top-scored sample among generated. We detail the parameters that were used to run classical docking models (AUTODOCK VINA (v1.2.5) (Trott & Olson, 2010), SMINA (v2020.12.10; fork of Vina 1.1.2) (Koes et al., 2013), and GNINA (v1.0.3) (McNutt et al., 2021)) in Appendix B.

**Pocket Detection for Classical Docking Methods** Classical docking methods and UNI-MOL face fundamental challenges in blind docking due to their reliance on pocket identification algorithms. This dependence introduces additional error when binding sites are unknown, representing a key limitation compared to end-to-end methods. We evaluate these methods using P2RANK (Krivák & Hoksza, 2018), FPOCKET (Le Guilloux et al., 2009), and whole protein approaches. Among these, P2RANK has shown the best performance and is used as the primary pocket detection method for our main results. The complete results are provided in Appendix C.1.2.

**MATCHA inference parameters** We run MATCHA in two inference regimes: in blind docking setup using all protein chains and in the pocket-aware scenario with the correct binding site provided. The first model in the pipeline generates 40 samples, which are then passed to the refinement stages. Then, the plausibility filtering is applied, reducing the number of candidate poses. We use the top-scored pose among the rest of the candidates.

## 4 RESULTS AND DISCUSSION

### 4.1 COMPREHENSIVE EVALUATION ON DIVERSE BENCHMARKS

We evaluate MATCHA against established baselines: classical docking (SMINA, VINA, GNINA), deep learning-based (DL-based) methods (DIFFDOCK, UNI-MOL, NEURALPLEXER and FLOWDOCK) as well as co-folding models (ALPHAFOLD 3, CHAI-1, BOLTZ-2). The results for DockGen

dataset as well as all extended results are reported in Appendix C.1. Additionally, we evaluate the considered models in the pocket-aware scenario with the corrected binding site location provided (see Appendix C.2).

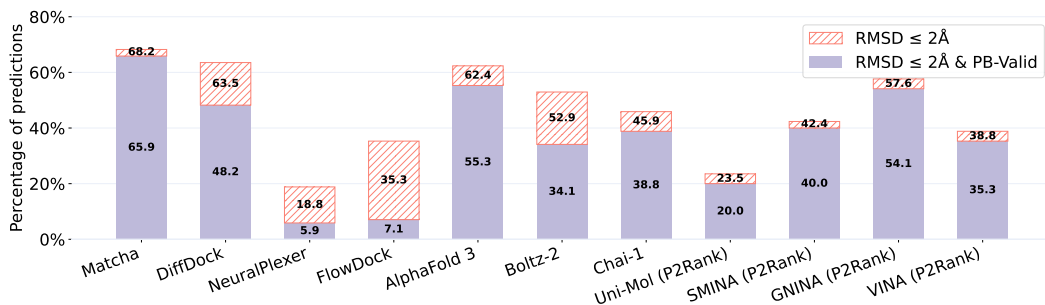


Figure 3: Blind ligand docking success rates on ASTEX Diverse Set ( $n = 85$ ).

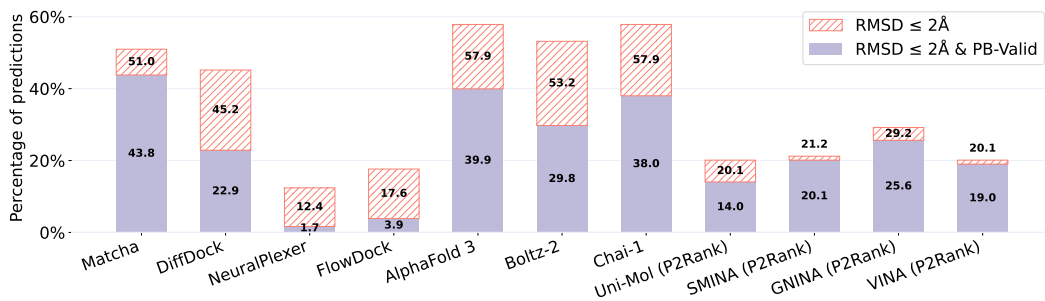


Figure 4: Blind ligand docking success rates on PDBBIND test set ( $n = 363$ ).

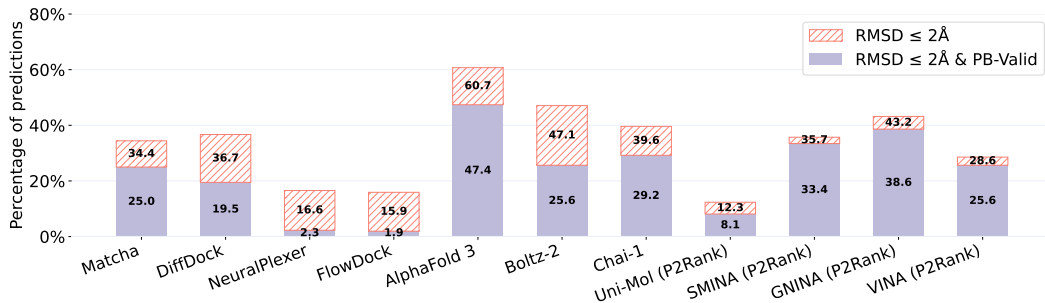


Figure 5: Blind ligand docking success rates on POSEBUSTERS V2 dataset ( $n = 308$ ).

On the ASTEX dataset, MATCHA demonstrates superior performance across all metrics, achieving the highest success rates for both  $\text{RMSD} \leq 2 \text{ \AA}$  (68.2%) and the harder  $\text{RMSD} \leq 2 \text{ \AA}$  & PB-valid (65.9%), outperforming the next-best method (ALPHAFOLD 3) by 10.6 percentage points on physically valid structures. The substantial improvement in the number of physically valid structures highlights the effectiveness of our flow matching approach in generating chemically plausible poses while maintaining high geometric accuracy.

On the PDBBIND test set, MATCHA demonstrates superior performance across all metrics compared to DL-based docking methods. While co-folding methods achieve slightly higher  $\text{RMSD} \leq 2 \text{ \AA}$  success rates, MATCHA shows the highest success rate of 43.8% for  $\text{RMSD} \leq 2 \text{ \AA}$  & PB-valid, surpassing even ALPHAFOLD 3 (39.9%). This demonstrates that MATCHA produces the most physically plausible and chemically valid structures, making it particularly valuable for practical drug discovery applications.

The POSEBUSTERS V2 dataset presents the most challenging evaluation scenario, where MATCHA’s performance shows a relative decrease compared to co-folding methods due to a higher proportion of protein targets with binding pockets structurally dissimilar to the training data (Morehead et al., 2025). Co-folding methods, trained on significantly larger and more diverse protein structure datasets, demonstrate better generalization to these out-of-distribution pocket geometries. Nevertheless, MATCHA maintains superior performance compared to other DL-based methods (DIFFDOCK-L, NEURALPLEXER, FLOWDOCK), confirming the effectiveness of our approach within the shared training distribution. This evaluation highlights the fundamental limitation of such models in generalizing beyond training data distributions.

## 4.2 COMPUTATIONAL EFFICIENCY OF MATCHA

**Inference Speed Analysis** We measure the average inference time for all considered blind docking methods on NVIDIA A100 40Gb GPU (see Figure 6). Time is measured only for model inference avoiding model loading. The exact timing results (in seconds) are detailed in Appendix H. MATCHA demonstrates the best speed-accuracy balance in terms of fraction of PoseBusters-valid predictions with  $\text{RMSD} \leq 2 \text{ \AA}$ , which is important in practical applications. MATCHA achieves substantially higher docking success rates compared to fast methods (DIFFDOCK-L, NEURALPLEXER, FLOWDOCK), having even faster inference time. Also, MATCHA shows a significant speed advantage over high-accuracy co-folding methods, achieving comparable docking quality.

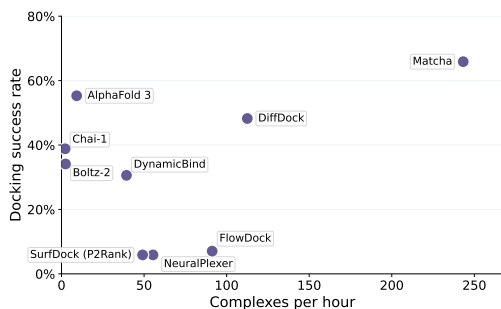


**Figure 6:** The dependence between the average docking inference time and percentage of PoseBusters-valid predictions for ASTEX dataset.

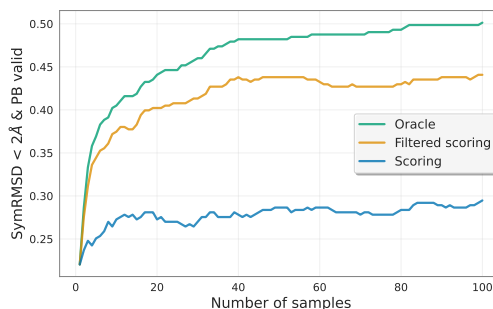


**Figure 7:** The dependence between the number of generated samples and MATCHA docking quality ( $\text{RMSD} \leq 2 \text{ \AA}$  & PB valid) for PDBBIND test set.

**Training speed** MATCHA required significantly less computational resources for training compared to competing methods: 38 GPU-days on a single H100 versus 120 GPU-days for DIFFDOCK-L (4× RTX A6000) and 3,840 GPU-days for CHAI-1 (128× A100). This highlights MATCHA’s efficiency in both training and inference compared to DL-based models and co-folding models.

## 4.3 ANALYSIS OF THE REQUIRED NUMBER OF SAMPLES

Figure 7 shows how the number of generated poses affects the quality of the best selected pose, comparing scoring-only regime, scoring with filtration (default), and oracle performance (representing the theoretical upper bound). Using scoring model increases  $\text{RMSD} \leq 2 \text{ \AA}$  & PB valid from 0.22 to 0.27, while adding physically-aware post-filtration improves results to 0.44, demonstrating the critical importance of incorporating molecular validity constraints alongside learned scoring functions. Performance plateaus at around 40 samples, marking the optimal computational cost-quality trade-off. The gap between filtered scoring and oracle performance indicates remaining opportunities for improvement in pose selection, while the convergence behavior suggests that the current sampling strategy effectively explores the relevant conformational space within the first 40 generated poses.

## 4.4 PHYSICAL VALIDITY ASSESSMENT

A critical advantage of MATCHA lies in its ability to generate physically plausible molecular poses. For instance, on the PDBBIND test set, MATCHA has 85.9% of physically-valid structures among

432 those with  $\text{RMSD} \leq 2 \text{ \AA}$ . To compare, ALPHAFOLD 3 has 68.9%, DIFFDOCK-L – 50.7%. This  
433 consistent superiority in generating chemically valid poses across different datasets demonstrates  
434 that MATCHA’s flow matching approach effectively preserves molecular constraints through two  
435 key mechanisms: (1) ligand parametrization using only torsional angles, which maintains internal  
436 molecular geometry, and (2) fast and effective post-filtration to eliminate unrealistic complex poses.  
437 The high fraction of physically plausible structures, combined with fast inference, makes MATCHA  
438 particularly suitable for practical drug discovery applications where chemical validity and screening  
439 efficiency are as important as geometric accuracy.

#### 441 4.5 IMPACT OF ALIGNMENT STRATEGY ON REPORTED METRICS

442 Pocket alignment refers to the procedure for superimposing predicted and reference protein–ligand  
443 complexes prior to RMSD evaluation, which is necessary for models that modify protein structure  
444 during prediction. Different strategies lead to systematically different results. One common option  
445 is the POCKET-BASED alignment, where the predicted pocket is aligned to the reference one. This  
446 can yield lower RMSD values even if the ligand is placed in a non-native binding site, effectively  
447 inflating success rates for both structure prediction and rigid docking methods. In contrast, we  
448 follow the BASE alignment strategy, in which the reference pocket is aligned to the full predicted  
449 protein, ensuring that incorrect pocket assignments are penalized. This methodological difference  
450 explains why our reported metrics may differ from those in other studies, even when using the  
451 same datasets. Appendix G provides a detailed comparison, showing that pocket-based alignment  
452 consistently increases success rates by 10–20% across methods, while leaving their relative ordering  
453 unchanged.

## 455 5 RELATED WORK

456  
457 Prior work on molecular docking can be organized along several orthogonal axes. One natural  
458 division is between classical heuristic-based approaches and modern deep learning methods. Within  
459 these, methods can be further distinguished by whether they treat docking as rigid-body alignment  
460 or as a co-folding process, and by whether they rely on discriminative or generative modeling of the  
461 complex.

462 Co-folding approaches represent some of the most computationally demanding directions in molec-  
463 ular docking, as they attempt to jointly predict the conformations of both proteins and ligands.  
464 Recent examples include ALPHAFOLD 3 (Abramson et al., 2024), CHAI-1 (Boitreaud et al., 2024),  
465 and BOLTZ-1/2 (Wohlwend et al., 2024; Passaro et al., 2025), NEURALPLEXER family (Qiao et al.  
466 2024b, Qiao et al. 2024a), INTERFORMER (Lai et al., 2024), DYNAMICBIND (Lu et al., 2024),  
467 LABIND (Zhang et al., 2025b), PHYSDOCK (Zhang et al., 2025a). These models are generally dif-  
468 fusion generative models in the Euclidean space. Since co-folding methods model protein positions,  
469 they typically require large-scale training and long inference time.

470 In contrast, rigid docking methods assume a fixed protein conformation and focus on placing a  
471 flexible ligand into binding site. This setting is computationally simpler than co-folding, yet it  
472 remains challenging due to the high dimensionality of ligand torsions and the rugged energy land-  
473 scape of protein pockets. Classical docking approaches, such as AUTODOCK VINA (Trott & Ol-  
474 son, 2010) and SMINA (Koes et al., 2013), rely on heuristic search combined with hand-crafted  
475 scoring functions. Recent deep learning methods reformulate rigid docking either as a regression  
476 problem or as generative modeling. Regression-based models, including EQUIBIND (Stärk et al.,  
477 2022), TANKBIND (Lu et al., 2022), E3BIND (Zhang et al., 2022), and FABIND (Pei et al., 2023),  
478 UNI-MOL (Alcaide et al., 2024), predict a single pose in one shot, often followed by torsional  
479 refinement of the ligand. Generative methods, such as DIFFDOCK (Corso et al., 2022) and FLOW-  
480 DOCK (Morehead & Cheng, 2025), instead learn distributions over poses and can sample diverse  
481 ligand conformations conditioned on the rigid receptor.

## 482 6 CONCLUSION

483  
484 We introduced MATCHA, a multi-stage Riemannian flow matching framework for molecular dock-  
485 ing that combines geometric generative modeling, scoring, and physical validity filtering. MATCHA

486 achieves a high physically valid docking accuracy while being substantially faster than many other  
487 models, making it suitable for large-scale applications. A key limitation is reduced generalization to  
488 unseen protein pockets, pointing to future work on receptor flexibility and broader protein coverage.  
489 Overall, MATCHA strikes a practical balance between accuracy, efficiency, and physical realism for  
490 structure-based drug discovery.

491  
492  
493  
494  
495  
496  
497  
498  
499  
500  
501  
502  
503  
504  
505  
506  
507  
508  
509  
510  
511  
512  
513  
514  
515  
516  
517  
518  
519  
520  
521  
522  
523  
524  
525  
526  
527  
528  
529  
530  
531  
532  
533  
534  
535  
536  
537  
538  
539

## 540 REFERENCES

- 541  
542 Josh Abramson, Jonas Adler, Jack Dunger, Richard Evans, Tim Green, Alexander Pritzel, Olaf  
543 Ronneberger, Lindsay Willmore, Andrew J Ballard, Joshua Bambrick, et al. Accurate structure  
544 prediction of biomolecular interactions with AlphaFold 3. *Nature*, 630(8016):493–500, 2024.
- 545 Eric Alcaide, Zhifeng Gao, Guolin Ke, Yaqi Li, Linfeng Zhang, Hang Zheng, and Gengmo Zhou.  
546 Uni-Mol docking V2: Towards realistic and accurate binding pose prediction. *arXiv preprint*  
547 *arXiv:2405.11769*, 2024.
- 548 Jacques Boitreaud, Jack Dent, Matthew McPartlon, Joshua Meier, Vinicius Reis, Alex Ro-  
549 gozhonikov, and Kevin Wu. Chai-1: Decoding the molecular interactions of life. *BioRxiv*, pp.  
550 2024–10, 2024.
- 551 Romain Brégier. Deep regression on manifolds: a 3D rotation case study. In *2021 International*  
552 *Conference on 3D Vision (3DV)*, pp. 166–174. IEEE, 2021.
- 553 Martin Buttenschoen, Garrett M Morris, and Charlotte M Deane. Posebusters: AI-based docking  
554 methods fail to generate physically valid poses or generalise to novel sequences. *Chemical Sci-*  
555 *ence*, 15(9):3130–3139, 2024.
- 556 Duanhua Cao, Mingan Chen, Runze Zhang, Zhaokun Wang, Manlin Huang, Jie Yu, Xinyu Jiang,  
557 Zhehuan Fan, Wei Zhang, Hao Zhou, et al. SurfDock is a surface-informed diffusion generative  
558 model for reliable and accurate protein–ligand complex prediction. *Nature Methods*, 22(2):310–  
559 322, 2025.
- 560 Ricky TQ Chen and Yaron Lipman. Flow matching on general geometries. *arXiv preprint*  
561 *arXiv:2302.03660*, 2023.
- 562 Vincent B Chen, W Bryan Arendall III, Jeffrey J Headd, Daniel A Keedy, Robert M Immormino,  
563 Gary J Kapral, Laura W Murray, Jane S Richardson, and David C Richardson. Molprobity: all-  
564 atom structure validation for macromolecular crystallography. *Acta Crystallographica Section*  
565 *Biological Crystallography*, 66(1):12–21, 2010. doi: 10.1107/S0907444909042073.
- 566 Gabriele Corso, Hannes Stärk, Bowen Jing, Regina Barzilay, and Tommi Jaakkola. DiffDock: Dif-  
567 fusion Steps, Twists, and Turns for Molecular Docking. *arXiv preprint arXiv:2210.01776*, 2022.
- 568 Gabriele Corso, Arthur Deng, Benjamin Fry, Nicholas Polizzi, Regina Barzilay, and Tommi  
569 Jaakkola. Deep confident steps to new pockets: Strategies for docking generalization. *ArXiv*,  
570 pp. arXiv–2402, 2024.
- 571 Warren L DeLano et al. Pymol: An open-source molecular graphics tool. *CCP4 Newsl. protein*  
572 *crystallogr.*, 40(1):82–92, 2002.
- 573 Sean R Eddy. Accelerated profile HMM searches. *PLoS computational biology*, 7(10):e1002195,  
574 2011.
- 575 Stefano Forli, Ruth Huey, Michael E Pique, Michel F Sanner, David S Goodsell, and Arthur J Olson.  
576 Computational protein–ligand docking and virtual drug screening with the autodock suite. *Nature*  
577 *protocols*, 11(5):905–919, 2016.
- 578 Forli Lab, CCSB, D. Santos-Martins, J. Eberhardt, and S. Forli. Meeko: Interface for  
579 AutoDock and RDKit. <https://meeko.readthedocs.io/> and <https://github.com/forlilab/Meeko>. Version 0.4.0, accessed 2025-09-11.
- 580 Richard A Friesner, Jay L Banks, Robert B Murphy, Thomas A Halgren, Jasna J Klicic, Daniel T  
581 Mainz, Matthew P Repasky, Eric H Knoll, Mee Shelley, Jason K Perry, et al. Glide: a new  
582 approach for rapid, accurate docking and scoring. 1. method and assessment of docking accuracy.  
583 *Journal of medicinal chemistry*, 47(7):1739–1749, 2004.
- 584 Michael J Hartshorn, Marcel L Verdonk, Gianni Chessari, Suzanne C Brewerton, Wijnand TM  
585 Mooij, Paul N Mortenson, and Christopher W Murray. Diverse, high-quality test set for the  
586 validation of protein–ligand docking performance. *Journal of medicinal chemistry*, 50(4):726–  
587 741, 2007.

- 594 Liegi Hu, Mark L Benson, Richard D Smith, Michael G Lerner, and Heather A Carlson. Binding  
595 MOAD (mother of all databases). *Proteins: Structure, Function, and Bioinformatics*, 60(3):333–  
596 340, 2005.
- 597 David Ryan Koes, Matthew P Baumgartner, and Carlos J Camacho. Lessons learned in empirical  
598 scoring with SMINA from the CSAR 2011 benchmarking exercise. *Journal of chemical informa-*  
599 *tion and modeling*, 53(8):1893–1904, 2013.
- 600 Radoslav Krivák and David Hoksza. P2Rank: machine learning based tool for rapid and accurate  
601 prediction of ligand binding sites from protein structure. *Journal of cheminformatics*, 10(1):39,  
602 2018.
- 603 Houtim Lai, Longyue Wang, Ruiyuan Qian, Junhong Huang, Peng Zhou, Geyan Ye, Fandi Wu, Fang  
604 Wu, Xiangxiang Zeng, and Wei Liu. Interformer: an interaction-aware model for protein-ligand  
605 docking and affinity prediction. *Nature Communications*, 15(1):10223, 2024.
- 606 Greg Landrum. RDKit: Open-Source Cheminformatics Software, 2024. URL [https://github.com/rdkit/rdkit/releases/tag/Release\\_2024\\_09\\_1](https://github.com/rdkit/rdkit/releases/tag/Release_2024_09_1). Release  
607 2024.09.1.
- 608 Vincent Le Guilloux, Peter Schmidtke, and Pierre Tuffery. Fpocket: an open source platform for  
609 ligand pocket detection. *BMC bioinformatics*, 10(1):168, 2009.
- 610 Zeming Lin, Halil Akin, Roshan Rao, Brian Hie, Zhongkai Zhu, Wenting Lu, Allan dos San-  
611 tos Costa, Maryam Fazel-Zarandi, Tom Sercu, Sal Candido, et al. Language Models of Protein  
612 Sequences at the Scale of Evolution Enable Accurate Structure Prediction. *bioRxiv*, 2022:500902,  
613 2022.
- 614 Yaron Lipman, Ricky TQ Chen, Heli Ben-Hamu, Maximilian Nickel, and Matt Le. Flow matching  
615 for generative modeling. *arXiv preprint arXiv:2210.02747*, 2022.
- 616 Zhihai Liu, Minyi Su, Li Han, Jie Liu, Qifan Yang, Yan Li, and Renxiao Wang. Forging the basis  
617 for developing protein–ligand interaction scoring functions. *Accounts of chemical research*, 50  
618 (2):302–309, 2017.
- 619 Ilya Loshchilov and Frank Hutter. Decoupled Weight Decay Regularization. *arXiv preprint*  
620 *arXiv:1711.05101*, 2017.
- 621 Wei Lu, Qifeng Wu, Jixian Zhang, Jiahua Rao, Chengtao Li, and Shuangjia Zheng. Tankbind:  
622 Trigonometry-aware neural networks for drug-protein binding structure prediction. *Advances in*  
623 *neural information processing systems*, 35:7236–7249, 2022.
- 624 Wei Lu, Jixian Zhang, Weifeng Huang, Ziqiao Zhang, Xiangyu Jia, Zhenyu Wang, Leilei Shi,  
625 Chengtao Li, Peter G Wolynes, and Shuangjia Zheng. DynamicBind: predicting ligand-specific  
626 protein-ligand complex structure with a deep equivariant generative model. *Nature Communica-*  
627 *tions*, 15(1):1071, 2024.
- 628 Andrew T McNutt, Paul Francoeur, Rishal Aggarwal, Tomohide Masuda, Rocco Meli, Matthew  
629 Ragoza, Jocelyn Sunseri, and David Ryan Koes. Gnina 1.0: molecular docking with deep learn-  
630 ing. *Journal of cheminformatics*, 13(1):43, 2021.
- 631 Alex Morehead and Jianlin Cheng. Flowdock: Geometric flow matching for generative protein-  
632 ligand docking and affinity prediction. *ArXiv*, pp. arXiv–2412, 2025.
- 633 Alex Morehead, Nabin Giri, Jian Liu, Pawan Neupane, and Jianlin Cheng. Deep learning for protein-  
634 ligand docking: Are we there yet? *ArXiv*, pp. arXiv–2405, 2025.
- 635 Saro Passaro, Gabriele Corso, Jeremy Wohlwend, Mateo Reveiz, Stephan Thaler, Vignesh Ram  
636 Somnath, Noah Getz, Tally Portnoi, Julien Roy, Hannes Stark, et al. Boltz-2: Towards accurate  
637 and efficient binding affinity prediction. *BioRxiv*, pp. 2025–06, 2025.
- 638 William Peebles and Saining Xie. Scalable diffusion models with transformers. In *Proceedings of*  
639 *the IEEE/CVF international conference on computer vision*, pp. 4195–4205, 2023.

- 648 Qizhi Pei, Kaiyuan Gao, Lijun Wu, Jinhua Zhu, Yingce Xia, Shufang Xie, Tao Qin, Kun He, Tie-  
649 Yan Liu, and Rui Yan. Fabind: Fast and accurate protein-ligand binding. *Advances in Neural*  
650 *Information Processing Systems*, 36:55963–55980, 2023.
- 651  
652 Zhuoran Qiao, Feizhi Ding, Thomas Dresselhaus, Mia A Rosenfeld, Xiaotian Han, Owen Howell,  
653 Aniketh Iyengar, Stephen Opalenski, Anders S Christensen, Sai Krishna Sirumalla, et al. Neu-  
654 ralplexer3: Accurate biomolecular complex structure prediction with flow models. *arXiv preprint*  
655 *arXiv:2412.10743*, 2024a.
- 656 Zhuoran Qiao, Weili Nie, Arash Vahdat, Thomas F Miller III, and Animashree Anandkumar. State-  
657 specific protein–ligand complex structure prediction with a multiscale deep generative model.  
658 *Nature Machine Intelligence*, 6(2):195–208, 2024b.
- 659 Sereina Riniker and Gregory A Landrum. Better informed distance geometry: using what we know  
660 to improve conformer generation. *Journal of Chemical Information and Modeling*, 55(12):2562–  
661 2574, 2015. doi: 10.1021/acs.jcim.5b00654.
- 662  
663 Ken Shoemake. Animating rotation with quaternion curves. In *Proceedings of the 12th annual*  
664 *conference on Computer graphics and interactive techniques*, pp. 245–254, 1985.
- 665 Hannes Stärk, Octavian Ganea, Lagnajit Pattanaik, Regina Barzilay, and Tommi Jaakkola. Equibind:  
666 Geometric deep learning for drug binding structure prediction. In *International conference on*  
667 *machine learning*, pp. 20503–20521. PMLR, 2022.
- 668  
669 Vladimir Sulimov, Ivan Ilin, Danil Kutov, and Alexey Sulimov. Development of docking programs  
670 for Lomonosov supercomputer. *Journal of the Turkish Chemical Society Section A: Chemistry*, 7  
671 (1):259–276, 2020.
- 672 Oleg Trott and Arthur J Olson. AutoDock Vina: improving the speed and accuracy of docking  
673 with a new scoring function, efficient optimization, and multithreading. *Journal of computational*  
674 *chemistry*, 31(2):455–461, 2010.
- 675  
676 Frank W Warner. *Foundations of differentiable manifolds and Lie groups*, volume 94. Springer  
677 Science & Business Media, 1983.
- 678 Jeremy Wohlwend, Gabriele Corso, Saro Passaro, Mateo Reveiz, Ken Leidal, Wojtek Swiderski,  
679 Tally Portnoi, Itamar Chinn, Jacob Silterra, Tommi Jaakkola, et al. Boltz-1: Democratizing  
680 biomolecular interaction modeling. *bioRxiv*, pp. 2024–11, 2024.
- 681  
682 J. M. Word, S. C. Lovell, J. S. Richardson, and D. C. Richardson. Asparagine and glutamine: using  
683 hydrogen atom contacts in the choice of side-chain amide orientation. *Journal of Molecular*  
684 *Biology*, 285(4):1735–1747, 1999. doi: 10.1006/jmbi.1998.2401.
- 685 Kexin Zhang, Yuanyuan Ma, Jiale Yu, Huiting Luo, Jinyu Lin, Yifan Qin, Xiangcheng Li, Qian  
686 Jiang, Fang Bai, Jiayi Dou, et al. PhysDock: A Physics-Guided All-Atom Diffusion Model for  
687 Protein-Ligand Complex Prediction. *bioRxiv*, pp. 2025–04, 2025a.
- 688  
689 Yangtian Zhang, Huiyu Cai, Chence Shi, Bozita Zhong, and Jian Tang. E3bind: An end-to-end  
690 equivariant network for protein-ligand docking. *arXiv preprint arXiv:2210.06069*, 2022.
- 691  
692 Zhijun Zhang, Lijun Quan, Junkai Wang, Liangchen Peng, Qiufeng Chen, Bei Zhang, Lexin Cao,  
693 Yelu Jiang, Geng Li, Liangpeng Nie, et al. LABind: identifying protein binding ligand-aware  
694 sites via learning interactions between ligand and protein. *Nature Communications*, 16(1):7712,  
2025b.
- 695  
696 Gengmo Zhou, Zhifeng Gao, Qiankun Ding, Hang Zheng, Hongteng Xu, Zhewei Wei, Linfeng  
697 Zhang, and Guolin Ke. Uni-Mol: A universal 3D molecular representation learning framework.  
698 2023.
- 699  
700  
701

## APPENDIX

A FLOW MATCHING ON  $SO(2)$  AND  $SO(3)$ 

In this section, we address the problem of training flow matching on the special orthogonal groups  $SO(2)$  and  $SO(3)$ . Our approach involves minimizing the flow matching loss function with respect to the parameters  $\mathbf{w}$  of a flow model denoted by  $v$ . The loss function is defined as:

$$\ell(\mathbf{w}) = \mathbb{E}_{\mathbf{x}_0, \mathbf{x}_1, t} \left\| v(\mathbf{x}(t), t; \mathbf{w}) - \frac{d\mathbf{x}(t)}{dt} \right\|_g, \quad (4)$$

In the equation above,  $\mathbf{x}(t)$  represents an interpolation between two points  $\mathbf{x}_0$  and  $\mathbf{x}_1$ . The term  $\|\mathbf{x}\|_g = \sqrt{g(\mathbf{x}, \mathbf{x})}$  defines a norm based on the Riemannian metric  $g$ .

For a given Riemannian manifold  $M$ , the tangent space at a point  $p \in M$  is denoted by  $\mathcal{T}_p M$ . The Riemannian metric is defined as:

$$g : \mathcal{T}_p M \times \mathcal{T}_p M \rightarrow \mathbb{R}, \quad (5)$$

acts on the Cartesian product of these tangent spaces to produce a non-negative scalar value.

The special orthogonal group  $SO(n)$  consists of elements that can be represented as  $n \times n$  rotation matrices. Although there are several ways to define a Riemannian metric  $g$  on  $SO(n)$ , the canonical metric is given by:

$$g(\mathbf{X}, \mathbf{Y}) \triangleq \text{tr}(\mathbf{X}^\top \mathbf{Y}), \quad (6)$$

where  $\mathbf{X}$  and  $\mathbf{Y}$  are  $n \times n$  matrices corresponding to the elements of the tangent space.

Regarding interpolation on these manifolds, various methods exist. In this work, we employ the widely used spherical linear interpolation, commonly referred to as SLERP Shoemake (1985).

A.1  $SO(2)$  MANIFOLD

Every  $2 \times 2$  rotation matrix is characterized by the rotation angle  $\theta$  and is given by

$$\mathbf{R} = \begin{bmatrix} \cos(\theta) & -\sin(\theta) \\ \sin(\theta) & \cos(\theta) \end{bmatrix}. \quad (7)$$

Given two rotation matrices defined by angles  $\theta_0$  and  $\theta_1$ , the SLERP interpolation between them for  $t \in [0, 1]$  is represented by the matrix  $\mathbf{R}(t)$  with the angle

$$\theta(t) = \theta_0 + t(\theta_1 - \theta_0) = \theta_0 + t\Delta\theta. \quad (8)$$

The time derivative of this matrix is

$$\dot{\mathbf{R}}(t) = \begin{bmatrix} -\sin(\theta(t)) & -\cos(\theta(t)) \\ \cos(\theta(t)) & -\sin(\theta(t)) \end{bmatrix} \Delta\theta, \quad (9)$$

which can be expressed as

$$\dot{\mathbf{R}}(t) = \mathbf{R}(t) \begin{bmatrix} 0 & -\Delta\theta \\ \Delta\theta & 0 \end{bmatrix}. \quad (10)$$

This form — a product of a rotation matrix and a skew-symmetric matrix — can be derived for any element of  $SO(n)$ , given that the tangent space of an identity  $SO(n)$  matrix is spanned by skew-symmetric  $n \times n$  matrices.

Assuming the neural network model  $\hat{v}$  for the flow takes as input  $\theta$  and  $t$ , and outputs a scalar  $\hat{v}(\theta, t)$ , we can represent the flow as

$$v(\mathbf{R}(t), t) = \mathbf{R}(t) \begin{bmatrix} 0 & -\hat{v}(\theta(t), t) \\ \hat{v}(\theta(t), t) & 0 \end{bmatrix}. \quad (11)$$

Utilizing the canonical metric (6), the norm difference becomes

$$\|v(\mathbf{R}(t), t) - \dot{\mathbf{R}}(t)\| = \sqrt{2} |\theta_1 - \theta_0 - \hat{v}(\theta(t), t)|. \quad (12)$$

Consequently, our objective to be minimized is

$$\ell(\mathbf{w}) = \mathbb{E}_{\theta_0, \theta_1, t} (\theta_1 - \theta_0 - \hat{v}(\mathbf{R}(t), t, \mathbf{w}))^2. \quad (13)$$

## A.2 $SO(3)$ MANIFOLD

In contrast to  $SO(2)$  case, SLERP for  $3 \times 3$  rotation matrices is more complicated, often requiring a transformation into quaternions (Brégier, 2021). Nonetheless, it is possible to compute the interpolated matrix  $\mathbf{R}(t)$  and its corresponding time derivative, which belongs to the tangent space of  $\mathbf{R}(t)$ , using automatic differentiation tools.

Every tangent vector of a point  $\mathbf{R} \in SO(3)$  can be expressed as

$$\mathbf{R} \begin{bmatrix} 0 & -k_z & k_y \\ k_z & 0 & -k_x \\ -k_y & k_x & 0 \end{bmatrix}. \quad (14)$$

Assuming that the values  $k_x, k_y, k_z$  describe the matrix  $\dot{\mathbf{R}}(t)$ , a neural network can be constructed to yield three outputs:  $v_x, v_y, v_z$ . The flow model becomes

$$v(\mathbf{R}(t), t) = \mathbf{R}(t) \begin{bmatrix} 0 & -v_z & v_y \\ v_z & 0 & -v_x \\ -v_y & v_x & 0 \end{bmatrix}. \quad (15)$$

For the  $SO(3)$  manifold, the square of norm in equation (4) evaluates to

$$2(k_x - v_x)^2 + 2(k_y - v_y)^2 + 2(k_z - v_z)^2. \quad (16)$$

To determine the values  $k_x, k_y, k_z$ , one can leverage automatic differentiation to compute  $\dot{\mathbf{R}}(t)$ . Subsequently, these values can be extracted from the expression  $\mathbf{R}^\top(t)\dot{\mathbf{R}}(t)$ .

## B HOW WE RUN CLASSICAL DOCKING

**Classical docking baseline parameters** We used AUTODOCK VINA (v1.2.5) (Trott & Olson, 2010), SMINA (v2020.12.10; fork of Vina 1.1.2) (Koes et al., 2013), and GNINA (v1.0.3) (McNutt et al., 2021). Unless noted otherwise, all runs used `exhaustiveness 64` and `seed 42`. Pocket centers were provided as described below; the search box was centered at each pocket center and sized to the RDKit conformer diameter of the ligand plus a 10 Å padding on all six sides (equivalently, `autobox_add 10` where applicable). To emulate blind docking we also used a large box centered on the protein with padding `autobox_add 16`.

**Ligand and receptor preparation for classical docking** Each ligand was prepared from a SMILES string: standardization and neutralization of charges, adjustment to pH 7 protonation rules, addition of explicit hydrogens, and 3D conformer generation with RDKit’s ETKDG method (Riniker & Landrum, 2015). Receptor proteins were hydrogenated with REDUCE (v4.13) using the `FLIP` option (Asparagine (Asn), Glutamine (Gln), Histidine (His) side-chain flips) (Word et al., 1999; Chen et al., 2010). For AutoDock-family tools, inputs were converted to PDBQT with MEEKO (v0.4.0) (Forli Lab, CCSB et al.).

## C EXTENDED RESULTS

### C.1 BLIND DOCKING

#### C.1.1 DOCKGEN RESULTS

We report blind docking success rates for ASTEX, POSEBUSTERS V2 and PDBBIND test sets in the main text in Section 4.1. In Figure 8, we present the results for DOCKGEN test set, which

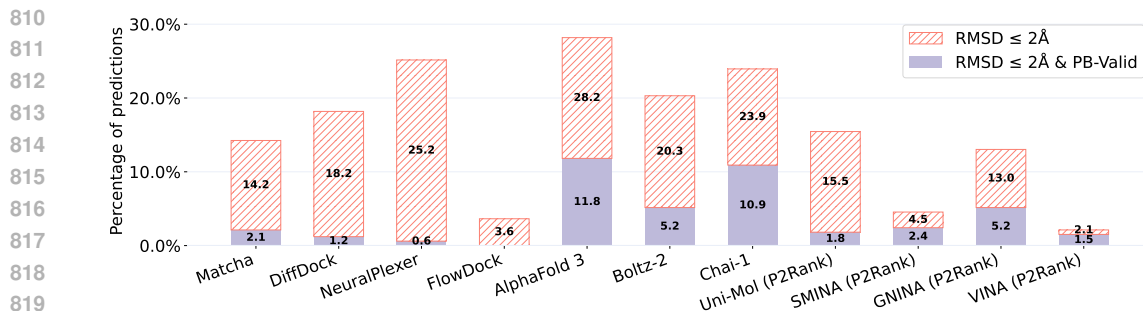


**Figure 8:** Blind ligand docking success rates on DOCKGEN dataset ( $n = 330$ ).

contains proteins with pockets that are structurally dissimilar to the training set. All considered models perform poorly on this set. However, co-folding models show better results. We explain it by the difference in training datasets: co-folding models have seen significantly more proteins during pre-training, which allows them to work better on the out-of-distribution proteins and ligands from the DOCKGEN dataset.

### C.1.2 RESULTS WITH DIFFERENT POCKET PREDICTION METHODS

In this section, we report results for blind docking scenario for models that require pocket information as input: UNI-MOL, SMINA, VINA, GNINA. We use three types of pocket information: P2RANK (Krivák & Hoksza, 2018), FPOCKET (Le Guilloux et al., 2009) and full protein setup. Full protein means providing the whole protein and the protein center as a starting pocket center: using large box centered on the protein with padding `autobox_add 16`. The full protein setup was not used for UNI-MOL because this model is unable to process such type of inputs.

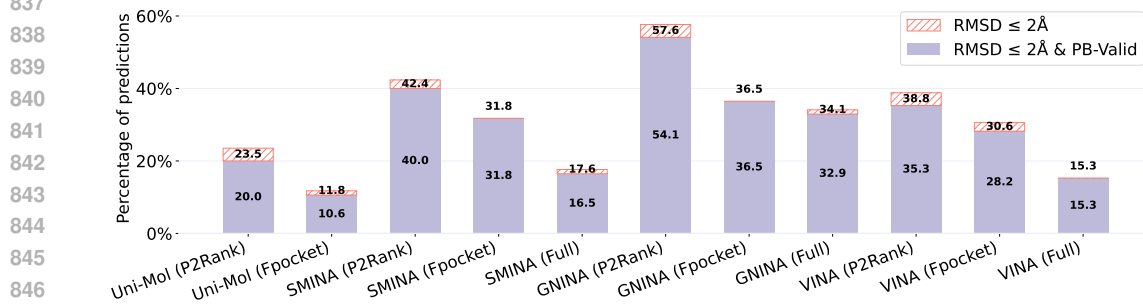


**Figure 9:** Blind ligand docking success rates with different pocket prediction methods on ASTEX Diverse set.

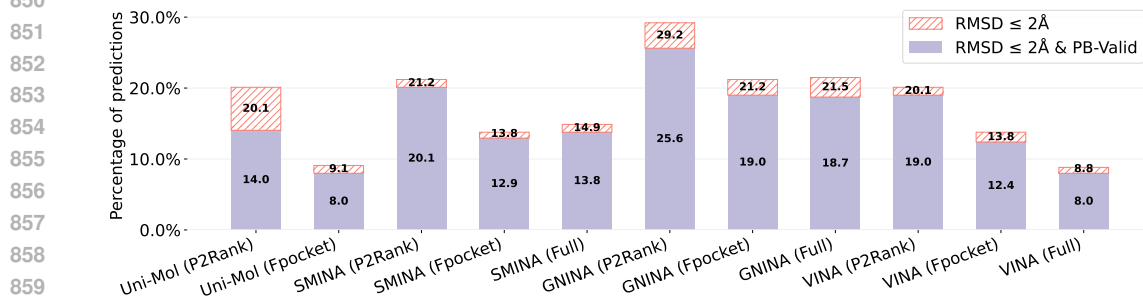


**Figure 10:** Blind ligand docking success rates with different pocket prediction methods on PDBBIND test set.

We report the results for all four considered test datasets in Figures 9, 10, 11, and 12. According to them, P2RANK consistently shows the best quality among all other pocket identification strategies.

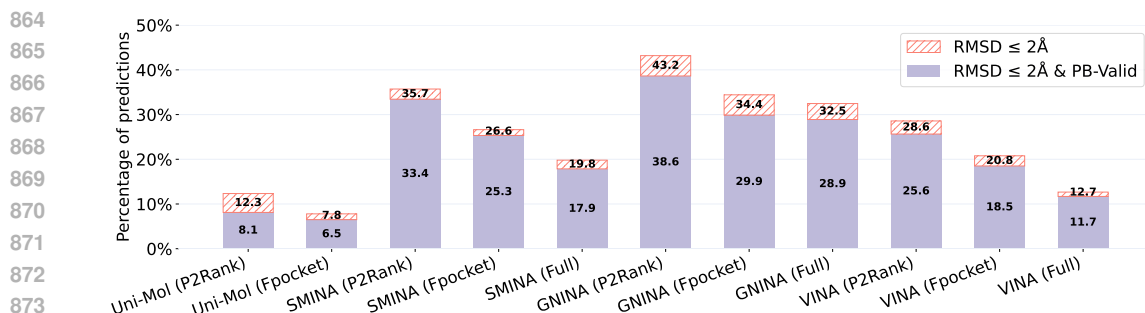


**Figure 11:** Blind ligand docking success rates with different pocket prediction methods on POSEBUSTERS V2 dataset.

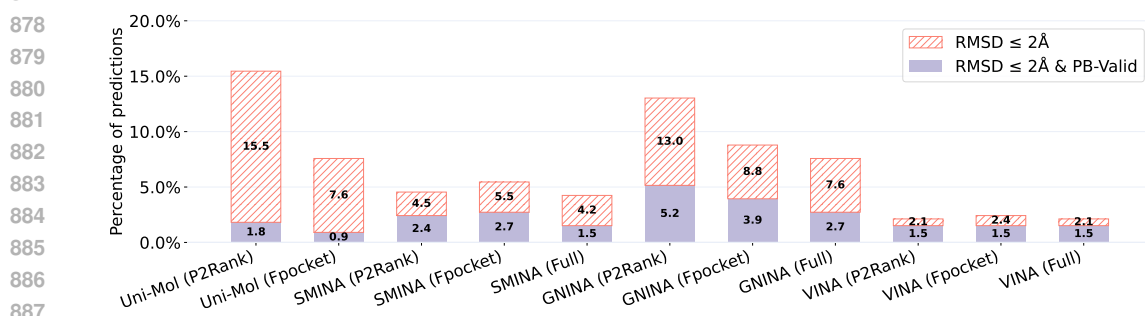


**Figure 12:** Blind ligand docking success rates with different pocket prediction methods on DOCKGEN dataset.

## C.2 POCKET-AWARE DOCKING

In addition to the blind docking setup, we run all models in the pocket-aware scenario, providing them with information about the true binding site (true ligand center). This scenario imitates the real-world case with the desired pocket for the protein provided. However, UNI-MOL cannot be fairly compared in the pocket-aware scenario due to its pocket cutting approach. Unlike other docking methods that can flexibly utilize pocket information as a starting point, UNI-MOL uses the provided reference pocket center to cut a small fixed-radius pocket around the ligand. This tight spatial constraint creates information leakage about the true ligand binding location, as the model becomes unable to "forget" or deviate significantly from the provided center due to the severely limited protein context. In contrast, methods like SMINA, VINA, GNINA, and MATCHA treat pocket information as a flexible starting point: they can explore and modify the binding site during their search process. Therefore, we do not report UNI-MOL results in the pocket-aware scenario.

In pocket-aware scenario with a known pocket center (stage 2 and stage 3 of MATCHA), we outperform classical docking tools on ASTEX, PDBBIND, DOCKGEN, but have slightly lower scores on POSEBUSTERS V2 due to the domain shift (Figures 13, 14, 15, and 16).

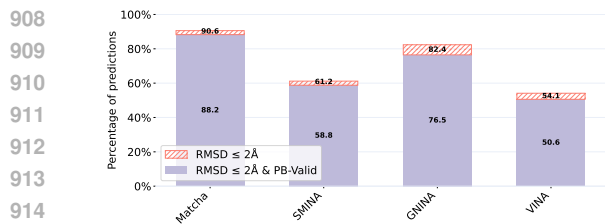


**Figure 13:** Pocket-aware ligand docking success rates on ASTEX Diverse set.

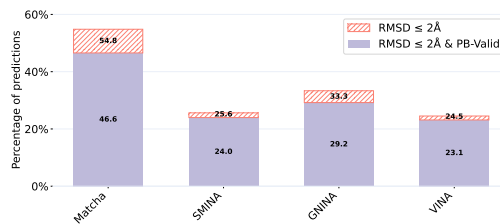


**Figure 14:** Pocket-aware ligand docking success rates on PDBBIND test set.

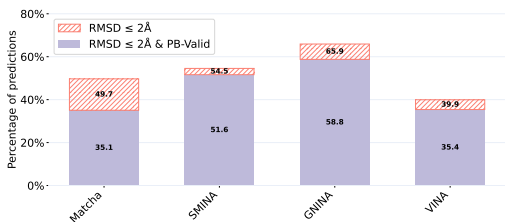


**Figure 15:** Pocket-aware ligand docking success rates on POSEBUSTERS V2 set.

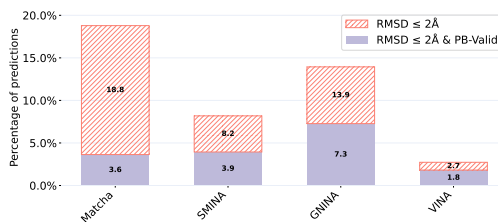


**Figure 16:** Pocket-aware ligand docking success rates on DOCKGEN test set.

## D ABLATION STUDIES

### D.1 PIPELINE ABLATION

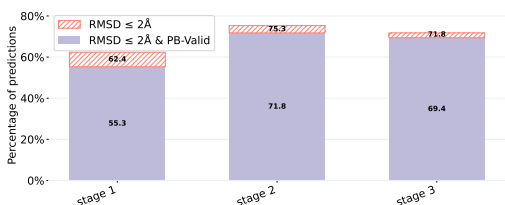


**Figure 17:** Blind ligand docking success rates after each pipeline step on ASTEX Diverse set.

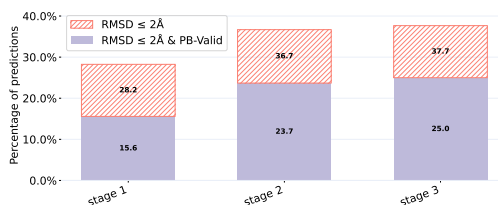


**Figure 18:** Blind ligand docking success rates after each pipeline step on POSEBUSTERS V2 dataset.

We report the results produced by each pipeline stage to demonstrate the effectiveness of a three-stage pipeline design and the improvements produced by each pipeline stage. The results are reported for ASTEX and POSEBUSTERS V2 datasets in Figures 17 and 18. The results demonstrate the effectiveness of a three-stage pipeline design: most complexes are successfully docked within the first two stages. Stage 3 is an additional low-noise refinement step that provides small improvements on complex datasets such as POSEBUSTERS V2.

### D.2 NUMBER OF INFERENCE STEPS



**Figure 19:** The dependence between the blind ligand docking success rates and number of Euler steps on ASTEX Diverse set.

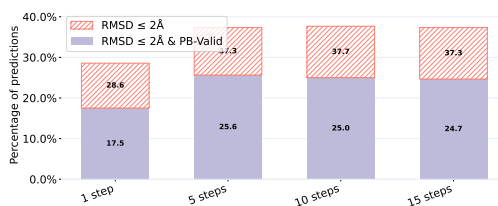


**Figure 20:** The dependence between the blind ligand docking success rates and number of Euler steps on POSEBUSTERS V2 dataset.

We conducted experiments to define the optimal number of Euler steps during inference. The results are reported for POSEBUSTERS V2 dataset in Figures 19 and 20. Increasing the number of Euler steps from 1 to 5 and then to 10 yields clear improvements in  $\text{RMSD} \leq 2 \text{ \AA}$  and  $\text{RMSD} \leq 2 \text{ \AA} \text{ \& PB-valid}$ . Beyond 10 steps, the gains saturate, and 15 steps do not provide measurable improvement.

## E COMPARISON TO NEW BASELINES

We computed docking quality metrics for two new baseline methods: DYNAMICBIND (Lu et al., 2024) and SURFDOCK (Cao et al., 2025), which use the equivariant geometric diffusion networks.

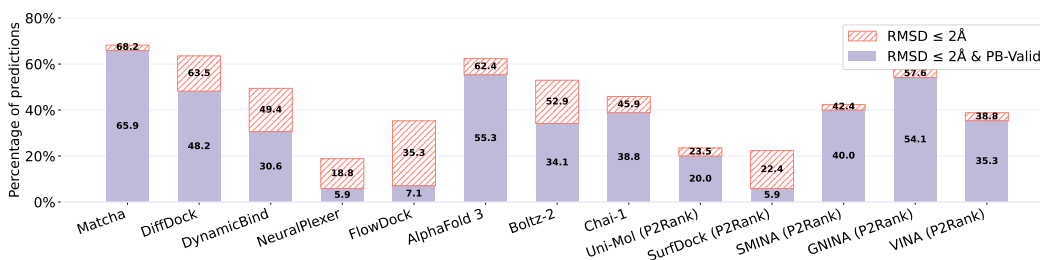


Figure 21: Blind ligand docking success rates on ASTEX Diverse set.

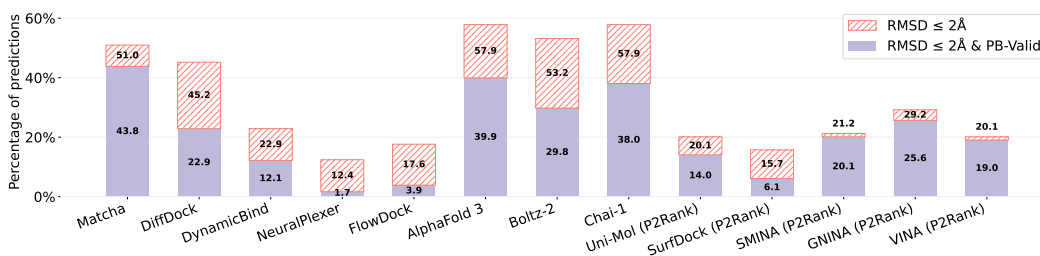


Figure 22: Blind ligand docking success rates on PDBBIND test set.

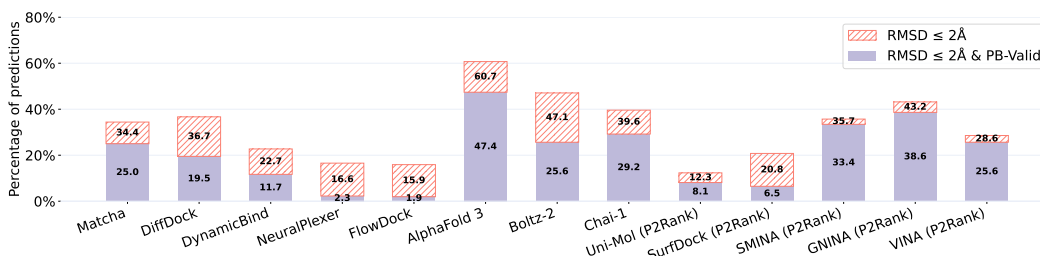


Figure 23: Blind ligand docking success rates on POSEBUSTERS V2 dataset.

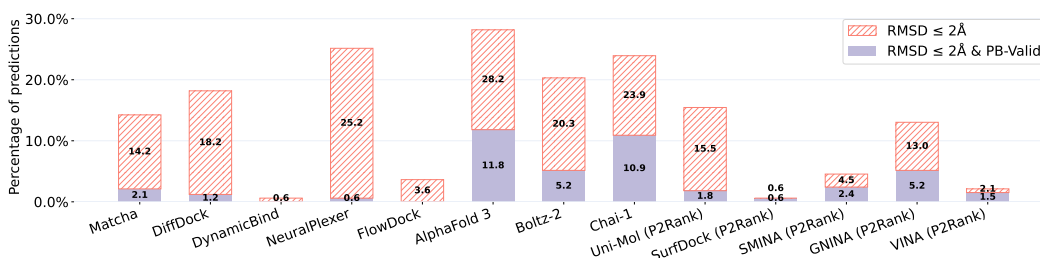
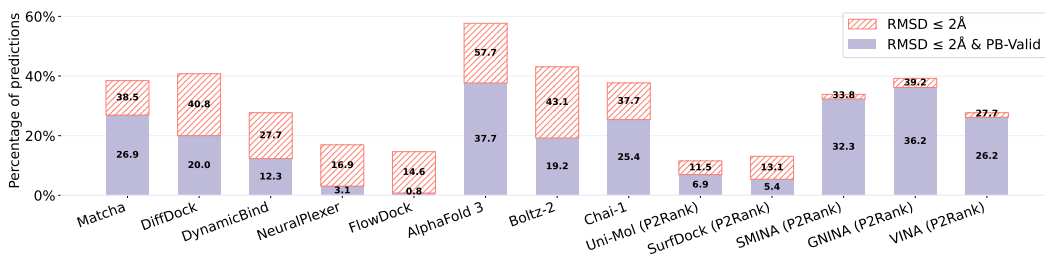


Figure 24: Blind ligand docking success rates on DOCKGEN dataset.

Since SURFDock is a pocket-based tool, we follow the same evaluation protocol as we used previously and use P2RANK to identify pockets. For both SURFDock and DYNAMICBIND we use experimentally-determined protein structures to be consistent with all previous evaluations. The results for all considered test datasets are shown in Figures 21, 22, 23, and 24. Across all test sets and both metrics ( $\text{RMSD} \leq 2 \text{ \AA}$  and  $\text{RMSD} \leq 2 \text{ \AA} \ \& \ \text{PB-valid}$ ), MATCHA consistently outperforms both DYNAMICBIND and SURFDock. We also compare inference speed (see Figure 6): the average runtime per complex is approximately 15 s for MATCHA, 91 s for DYNAMICBIND, and 73 s for SURFDock. Thus, MATCHA is not only more accurate on these benchmarks, but also considerably faster at inference.

## F BENCHMARKING ON UNSEEN POSEBUSTERS SPLIT



**Figure 25:** Blind ligand docking success rates on the subset of POSEBUSTERS V2 dataset with 130 / 308 complexes.

Following POSEBENCH (Morehead et al., 2025), we exclude POSEBUSTERS V2 complexes that were present in the ALPHAFOLD3 training set. It is caused by the fact that ALPHAFOLD3 and other co-folding models were trained on September 30, 2021 cutoff of PDBBIND, while POSEBUSTERS V2 uses complexes after 2019. Our model was trained on 2019 cutoff, and we used all 308 complexes for testing. Figure 25 presents results on the subset of POSEBUSTERS V2 ( $n=130$ ) which was deposited in the PDB after September 30, 2021. According to them, co-folding models show decrease in performance (up to 10% in  $\text{RMSD} \leq 2 \text{ \AA}$  & PB-valid) compared to the quality on the full ( $n=308$ ) set (see Figure 23). At the same time, MATCHA and other methods, both DL-based and classical docking, keep the performance at the same level. This fact indicates overoptimistic results for co-folding models shown on POSEBUSTERS V2 dataset due to the overlap with the training data.

## G THE IMPORTANCE OF THE POCKET ALIGNMENT

## G.1 POCKET-ALIGNED RMSD COMPUTATION

For all models that predict the structure of the whole complex, we follow Abramson et al. (2024) and use pocket-aligned symmetric RMSD. However, since this procedure is not clearly defined in the paper, we explain in detail how we perform the BASE pocket alignment.

1. The primary protein chain with the most atoms within  $10 \text{ \AA}$  of the ligand is kept.
2. The pocket is defined as all  $C_{\alpha}$  atoms within  $10 \text{ \AA}$  of any heavy atom of the reference ligand, restricted to protein backbone atoms.
3. The reference pocket is aligned to the *whole predicted protein structure* by  $C_{\alpha}$  atoms in PyMOL (DeLano et al., 2002) with *five refinement cycles*, which is the default parameter.

An alternative approach to compute pocket-aware RMSD was described in Qiao et al. (2024a). This POCKET-BASED approach shares the first two stages, but then the procedure differs:

3. The predicted pocket is defined as all  $C_{\alpha}$  atoms within  $10 \text{ \AA}$  of any heavy atom of the predicted ligand, restricted to protein backbone atoms.
4. *Each chain in the predicted pocket* is aligned to the reference pocket, and the chain with the minimum alignment RMSD is selected. The alignment is performed with *zero refinement cycles*.

We believe the base approach provides fair evaluation, while the pocket-based approach produces overoptimistic results due to a fundamental flaw: for multi-chain proteins with multiple binding sites it can artificially align non-corresponding pockets with low RMSD by chance. This allows predicted ligands to appear correctly positioned even when docked to entirely wrong pockets.

The pocket-based alignment artificially constrains translation error since pockets are pre-aligned, masking true docking failures that would be evident in blind docking scenarios. In contrast, real-world docking can produce large translation errors when ligands bind to incorrect sites—a critical failure mode that pocket-based metrics cannot detect.

This methodological difference explains the discrepancy between our metrics and those reported for ALPHAFOLD 3 in the NEURALPLEXER 3 (Qiao et al., 2024a) paper on the POSEBUSTERS V2 dataset. To demonstrate this bias, we show that rigid docking approaches can achieve the same artificial metric improvements when evaluated using pocket-based alignment. We demonstrate the comparison between the base and the pocket-based approaches in Appendix G.2.

## G.2 DOCKING RESULTS FOR DIFFERENT WAYS OF COMPUTING POCKET-ALIGNED RMSD

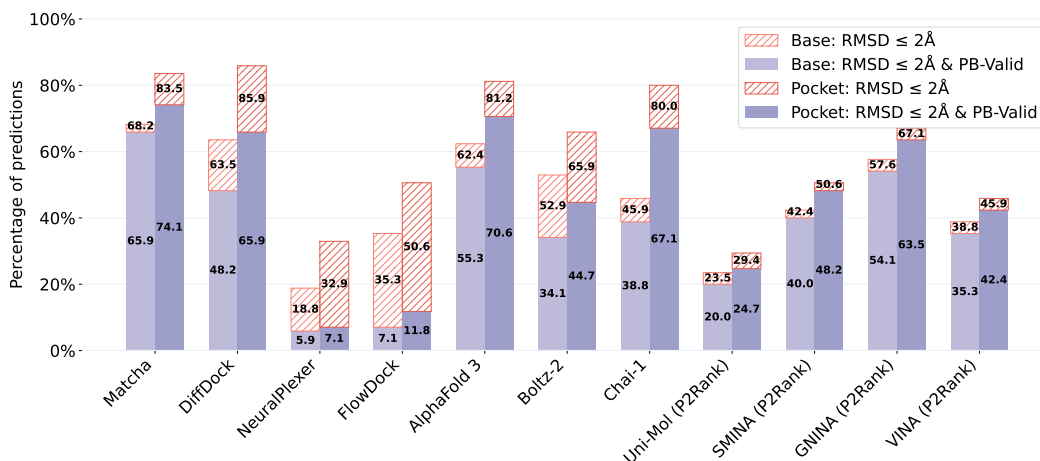


**Figure 26:** Comparison of pocket alignment strategies in blind docking scenario for ASTEX Diverse set.

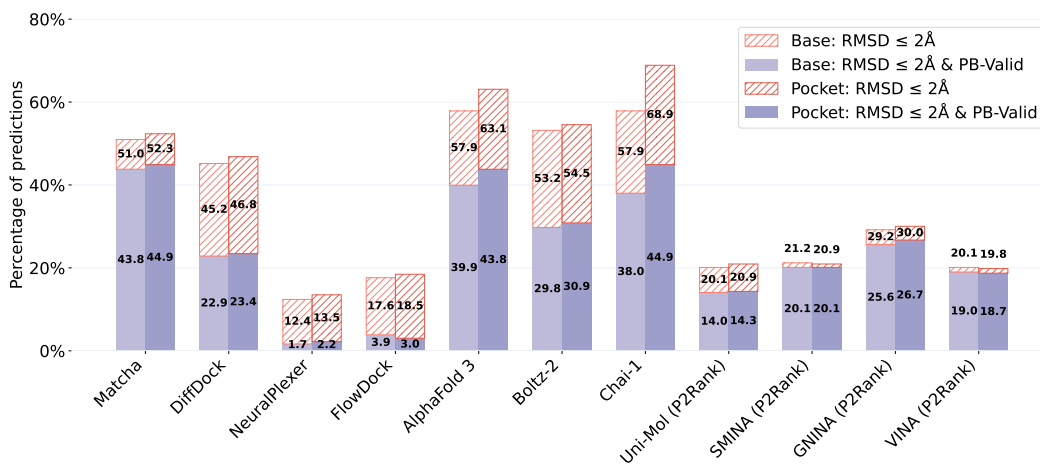


**Figure 27:** Comparison of pocket alignment strategies in blind docking scenario for PDBBIND test set.

We computed docking quality metrics using both base and pocket-based approaches for structure prediction methods (ALPHAFOLD 3, BOLTZ-2, CHAI-1, NEURALPLEXER, FLOWDOCK) and rigid docking approaches (DIFFDOCK-L, MATCHA). The results for all considered test datasets are shown in Figures 26, 27, 28, and 29. The obtained results reveal comparable metric inflation across all methods. This applies to all four test sets. The increase is around 15-20% in  $\text{RMSD} \leq 2\text{\AA}$  for the ASTEX dataset and around 10% for POSEBUSTERS V2. Lower increases for PDBBIND and DOCKGEN test sets are due to the use of the preprocessed dataset versions with the removed irrelevant chains provided by Corso et al. (2024). Moreover, the choice of the alignment almost does not affect the ordering of the docking methods: all our claims done for the base alignment, still hold for the pocket-based alignment. This demonstrates that the apparent superiority of co-folding methods in some evaluations may stem from evaluation methodology rather than genuine performance differences.

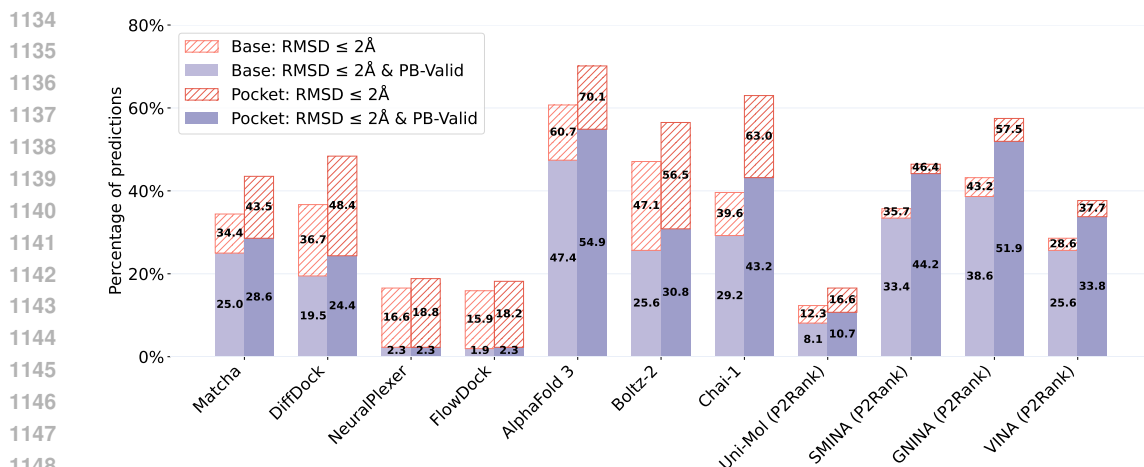


**Figure 28:** Comparison of pocket alignment strategies in blind docking scenario for POSEBUSTERS V2 dataset.

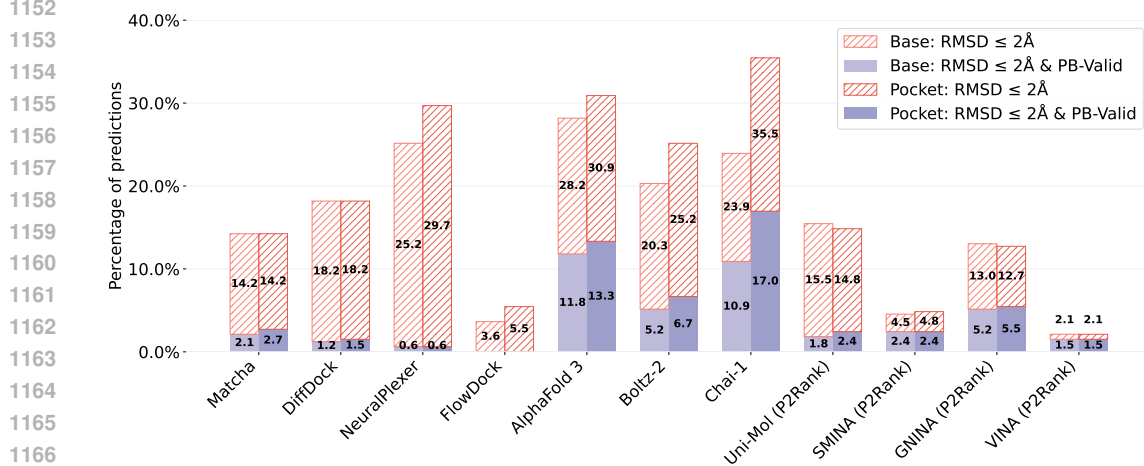


**Figure 29:** Comparison of pocket alignment strategies in blind docking scenario for DOCKGEN dataset.

## H INFERENCE SPEED COMPARISON

**Table 1:** Comparison of the average inference time for blind docking models (for ASTEX test set)

Method	Inference time (sec)
MATCHA	15
DIFFDOCK-L	32
NEURALPLEXER	65
FLOWDOCK	39
ALPHA FOLD 3	392
CHAI-1	1638
BOLTZ-2	1488

We report the average inference speed for all considered blind docking methods on one NVIDIA A100 40GB GPU. We use ASTEX dataset to measure the time on it. Time is reported only for model inference avoiding model loading. Most docking models generate multiple poses and select a pose with the best score, so we measure the time required to sample all required poses. The results are shown in Table 1.

1188 I POSEBUSTERS TESTS  
1189

1190 We report PoseBusters results for the following 27 tests according to the release in [https://](https://github.com/maabuu/posebusters/releases/tag/v0.4.5)  
1191 [github.com/maabuu/posebusters/releases/tag/v0.4.5](https://github.com/maabuu/posebusters/releases/tag/v0.4.5):  
1192

- 1193 1. mol\_pred\_loaded,
  - 1194 2. mol\_cond\_loaded,
  - 1195 3. sanitization,
  - 1196 4. inchi\_convertible,
  - 1197 5. all\_atoms\_connected,
  - 1198 6. bond\_lengths,
  - 1200 7. bond\_angles,
  - 1201 8. internal\_steric\_clash,
  - 1202 9. aromatic\_ring\_flatness,
  - 1203 10. non-aromatic\_ring\_non-flatness,
  - 1204 11. double\_bond\_flatness,
  - 1205 12. internal\_energy,
  - 1206 13. protein-ligand\_maximum\_distance,
  - 1207 14. minimum\_distance\_to\_protein,
  - 1208 15. minimum\_distance\_to\_organic\_cofactors,
  - 1209 16. minimum\_distance\_to\_inorganic\_cofactors,
  - 1210 17. minimum\_distance\_to\_waters,
  - 1211 18. volume\_overlap\_with\_protein,
  - 1212 19. volume\_overlap\_with\_organic\_cofactors,
  - 1213 20. volume\_overlap\_with\_inorganic\_cofactors,
  - 1214 21. volume\_overlap\_with\_waters,
  - 1215 22. double\_bond\_stereochemistry,
  - 1216 23. mol\_true\_loaded,
  - 1217 24. molecular\_bonds,
  - 1218 25. molecular\_formula,
  - 1219 26.  $\text{RMSD} \leq 2 \text{ \AA}$ ,
  - 1220 27. tetrahedral\_chirality.
- 1221  
1222  
1223  
1224  
1225  
1226  
1227  
1228  
1229  
1230  
1231  
1232  
1233  
1234  
1235  
1236  
1237  
1238  
1239  
1240  
1241